

# Quantifying the net slab pull force as a driving mechanism for plate tectonics

W. P. Schellart

School of Geosciences, Monash University, Melbourne, Victoria, Australia

Received 19 January 2004; revised 8 February 2004; accepted 20 February 2004; published 7 April 2004.

[1] It has remained unclear how much of the negative buoyancy force of the slab ( $F_B$ ) is used to pull the trailing plate at the surface into the mantle. Here I present three-dimensional laboratory experiments to quantify the net slab pull force ( $F_{NSP}$ ) with respect to  $F_B$  during subduction. Results show that  $F_{NSP}$  increases with increasing slab length and dip up to  $\sim 8$ – $12\%$  of  $F_B$ , making  $F_{NSP}$  up to twice as large as the ridge push force. The remainder of  $F_B$  is primarily used to drive rollback-induced mantle flow ( $\sim 70\%$ ), to bend the subducting plate at the trench ( $\sim 15$ – $30\%$ ) and to overcome shear resistance between slab and mantle ( $0$ – $8\%$ ). **INDEX TERMS:** 8120 Tectonophysics: Dynamics of lithosphere and mantle—general; 8121 Tectonophysics: Dynamics, convection currents and mantle plumes; 8122 Tectonophysics: Dynamics, gravity and tectonics; 8155 Tectonophysics: Plate motions—general; 8164 Tectonophysics: Stresses—crust and lithosphere. **Citation:** Schellart, W. P. (2004), Quantifying the net slab pull force as a driving mechanism for plate tectonics, *Geophys. Res. Lett.*, 31, L07611, doi:10.1029/2004GL019528.

## 1. Introduction

[2] Plate tectonic theory provides explanations for numerous large-scale features on Earth, such as mid-oceanic ridges, trenches and mountain chains. The theory is well established and its kinematic framework is generally accepted. However, considerable debate remains about the driving forces of the tectonic plates and their relative contribution. Important forces that have been proposed are slab pull, ridge push, trench suction and mantle drag [Elsasser, 1971; Forsyth and Uyeda, 1975]. It is generally thought that the main driving force for plate tectonics is the slab pull force, resulting from the negative buoyancy of the subducted slab compared to the surrounding mantle, and to a lesser extent the ridge push force, resulting from the excess potential energy of mid-oceanic ridges [Forsyth and Uyeda, 1975]. Calculations indicate that the ridge push force is  $\sim 2$ – $3 \times 10^{12}$  N/m [Parsons and Richter, 1980]. The total slab pull force is thought to be an order of magnitude larger than the ridge push force [Forsyth and Uyeda, 1975]. However, an unknown part of the slab pull force is balanced by viscous tractions in the mantle, thus making it difficult to quantify how much of this force is transmitted from the sinking slab across the subduction hinge towards the surface part of the subducting plate (e.g., net slab pull force). Also, it is unclear how much of the slab pull force can be transmitted across the subduction zone hinge, because hinges are not stable features but migrate (mostly retreat) through time [Garfunkel et

al., 1986]. Here I present results of three-dimensional fluid dynamic experiments to quantify the contribution of lithospheric subduction in driving plate tectonics and mantle flow. The magnitude of the net slab pull force is quantified for progressive time-steps and is compared with the total negative buoyancy force of the slab. Other forces resisting subduction are also investigated and quantified.

## 2. Model Set-Up

[3] The experiments are scaled as such that gravitational driving forces and viscous resistive forces are properly scaled and closely reflect the force balance in nature. The models consist of a high-viscosity ( $2.4 \times 10^4$  Pa-s) high-density ( $1.52 \times 10^3$  kg/m<sup>3</sup>) layer (silicone putty), overlying a low-viscosity ( $1.3 \times 10^2$  Pa-s) lower-density ( $1.42 \times 10^3$  kg/m<sup>3</sup>) layer (glucose syrup), contained in a rectangular box (Figure 1). The upper layer is 1.3–2.0 cm thick, simulating a 65–100 km thick subducting oceanic lithosphere. The layer is either fixed or free at its trailing edge, representing maximum and minimum resistance to lateral displacement. This allows  $F_{NSP}$  to be determined for these two extreme scenarios, which encompass the possible subduction scenarios on Earth. The lower layer is  $\sim 12$  cm thick, simulating  $\sim 600$  km of sub-lithospheric upper mantle. The bottom of the box represents the upper-lower mantle seismological discontinuity, which retards subduction. In nature, viscosity increases by a factor of  $\sim 30$  whilst crossing the discontinuity [Davies and Richards, 1992], which will significantly retard or stop further penetration [Fukao et al., 2001], and will make any contribution to slab pull from slab material in the lower mantle negligible [Conrad and Lithgow-Bertelloni, 2002]. Thus, in nature, the net slab pull force will result almost exclusively from the slab part in the upper mantle, which is simulated in the physical model. The viscosity ratio ( $\eta_{sp}/\eta_m \approx 185$ ) and density contrast ( $\Delta\rho = 100$  kg/m<sup>3</sup>) in the model reflect natural conditions ( $\eta_{sp}/\eta_m \approx 50$ – $200$  and  $\Delta\rho \approx 80$  kg/m<sup>3</sup>) [Cloos, 1993; Houseman and Gubbins, 1997; Conrad and Hager, 1999]. The applied time-scale ratio  $t^a/t^n$  is  $3.8 \times 10^{-12}$  (1 hour represents 30 Myr) and the applied length-scale ratio  $x^a/x^n$  is  $2.0 \times 10^{-7}$  (1 cm represents 50 km). Superscripts  $a$  and  $n$  refer to analogue model and nature respectively. Using the model upper mantle viscosity  $\eta_m \approx 1.3 \times 10^2$  Pa-s and the scale relationship ( $\eta^a/\eta^n = (\Delta\rho^a t^a x^a / \Delta\rho^n t^n x^n)$ ), this results in an upper mantle viscosity of  $\eta^n \approx 1.4 \times 10^{20}$  Pa-s, which is similar to viscosity values for the natural prototype ( $10^{19}$ – $10^{21}$  Pa-s) [Artyushkov, 1983; Ranalli, 1995].

[4] To visualize deformation and flow in the experiments, passive markers were placed in the silicone plate and in the syrup. At the start of the experiment, a subduction instability was produced manually at the tip of the slab by downward bending of a finite length of slab ( $\sim 2$  cm) at an

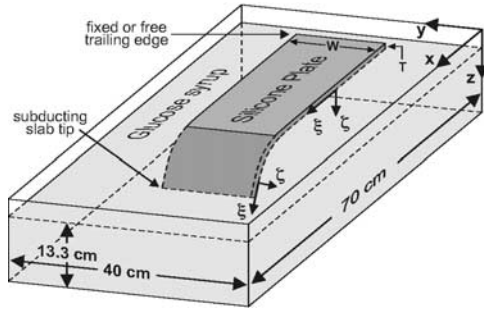


**Figure 1.** Configuration of the modeling apparatus and experimental set-up with a fixed or free trailing edge boundary condition.

angle of  $15\text{--}30^\circ$ . The system was then allowed to evolve naturally. The overriding plate was not modeled to trace subduction-induced flow. Thus, the subduction fault has the same strength as the sub-lithospheric mantle material. Although this is a low strength, previous investigations imply that the subduction fault is relatively weak [Gurnis and Hager, 1988; Conrad and Hager, 1999].

### 3. Model Results

[5] Experimental results are shown in Figure 2 for two reference experiments with either a fixed or free trailing edge. Slab sinking and hinge-retreat increase exponentially during subduction, with a gradual increase in slab dip from  $15\text{--}30^\circ$  up to  $\sim 60\text{--}80^\circ$ . Subsequently, subduction slows down when the slab tip hits the lower discontinuity. Slab retreat forces mantle material to flow around the lateral slab edges towards the mantle wedge. The slab transmits tensional stresses to the trailing part of the subducting plate during sinking. This can be deduced from the observed extensional strain in the surface part of the lithosphere for the fixed trailing edge experiment (Figures 2a and 2b) and from displacement of the trailing edge for the free trailing edge experiment (Figures 2c and 2d).

### 4. Driving and Resistive Forces in Experiments

[6] The only driving force present in the experiments is the negative buoyancy of the slab ( $F_B$ ), which drives subduction, plate deformation and mantle flow.  $F_B$  is balanced by the resistive forces on the slab:

$$F_B = F_I + F_{SH}(s) + F_{Be} + F_{RIF} + F_{NSP} \quad (1a)$$

with:

$$F_{NSP} = F_E + F_{SH}(h) \quad (1b)$$

The resistive forces include the inertial force ( $F_I$ ) (to accelerate the sinking slab), a viscous shear traction force ( $F_{SH}(s)$ ) (to displace the slab parallel to its plane), the bending force ( $F_{Be}$ ) (to bend the subducting plate), the rollback-induced flow force ( $F_{RIF}$ ) (to drive flow in the mantle due to slab perpendicular displacement (rollback)) and the net slab pull force ( $F_{NSP}$ ) (to pull the trailing plate into the subduction zone).  $F_{NSP}$  consists of two components, the extension force ( $F_E$ ) (to extend the trailing

plate (only for fixed trailing edge experiments)) and a viscous shear traction force ( $F_{SH}(h)$ ) (to displace the trailing plate parallel to its plane). The progressive development of the forces in equation (1a) has been illustrated in Figure 3 for the two reference experiments and will be discussed below.

[7] The slab buoyancy force ( $F_B$ ) was calculated from the product of  $\Delta\rho$ , slab volume  $V$  and the gravitational acceleration  $g$ .  $V$  is dependent on the slab length, which was measured from the slab tip to the trench.  $F_B$  was calculated from initiation of subduction until the slab tip hit the upper-lower mantle boundary. From this stage onward, an unknown part of  $F_B$  was supported by the boundary. As can be seen in Figure 3a, the magnitude of  $F_B$  increases with time due to the increase in slab length.

[8] From the resistive forces, the inertial force ( $F_I$ ) was negligible, because the acceleration of the slab ( $a_s$ ) was very small. A typical value for  $a_s$  of  $\sim 2.4 \times 10^{-7} \text{ m/s}^2$  for experiment 9 results in  $F_I/F_B \approx 3.7 \times 10^{-7}$ , indicating that the inertial force can be neglected.

[9] The viscous shear traction force ( $F_{SH}$ ) results from shearing between the subducting plate and the sub-lithospheric mantle due to plate-parallel displacement (modified from Jacoby [1973]):

$$F_{SH} = \eta_m A_s \frac{d}{d\zeta} \left( \frac{d\xi}{dt} \right) + \eta_m A_h \frac{d}{d\zeta} \left( \frac{d\xi}{dt} \right) \quad (2)$$

where  $\eta_m$  is the viscosity of the sub-lithospheric mantle;  $A_s$  is the total area of the slab in contact with the glucose syrup;  $\zeta$  and  $\xi$  indicate a direction in the  $xz$ -plane, everywhere perpendicular and parallel to the plate, respectively (Figure 1);  $t$  indicates time; and  $A_h$  is the area of the surface part of the plate in contact with the glucose syrup. Here,  $d\xi/dt$  indicates the plate-parallel velocity, while  $d/d\zeta$

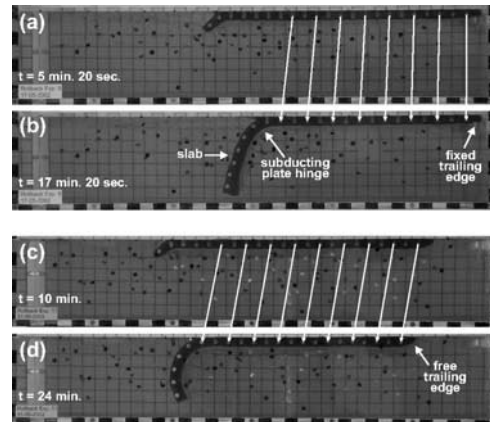


**Figure 2.** Side view images of experimental results during progressive subduction of a high-viscosity plate into a low viscosity layer, with (a) and (b) for experiment 9 (fixed trailing edge), and (c) and (d) for experiment 11 (free trailing edge). Long white arrows indicate displacement of passive markers in the side of the plate, pointing to horizontal extension of the plate for experiment 9 (differential displacement of markers) and horizontal translation of the plate for experiment 11 (constant displacement of markers).

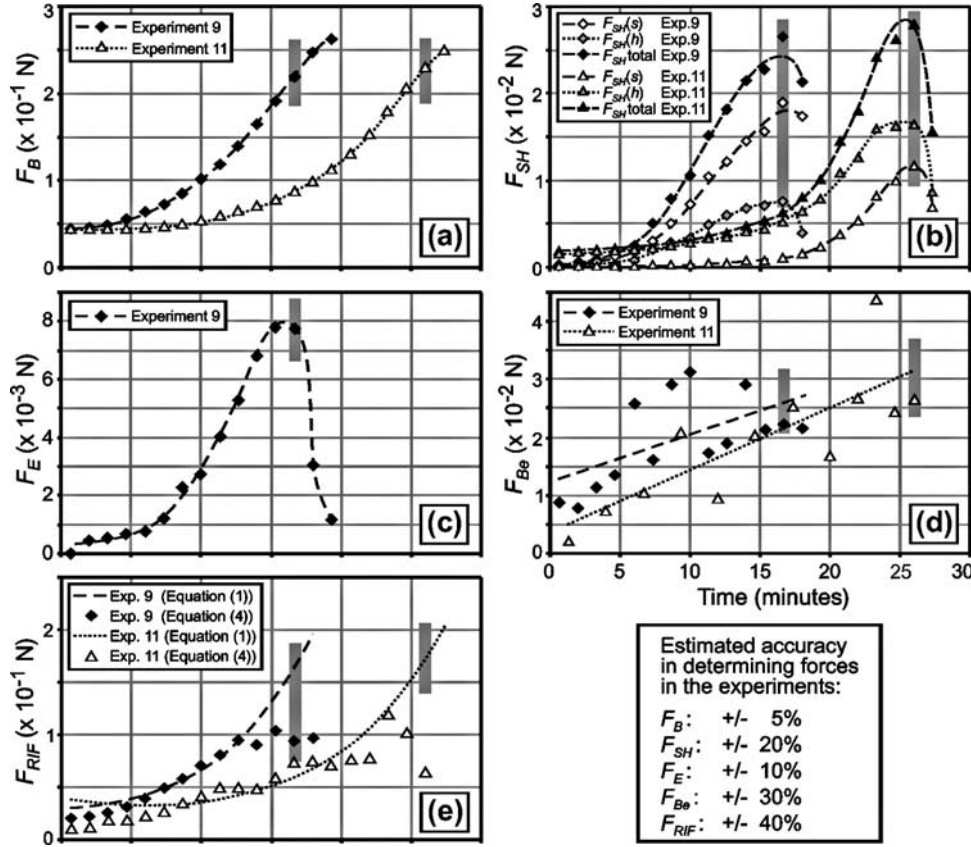


**Figure 3.** Diagrams illustrating the development of the driving force and most important resistive forces in experiments 9 and 11. (a) Buoyancy force of the slab ( $F_B$ ), (b) shear force between subducting plate and surrounding mantle material ( $F_{SH}$ ), (c) extension force in the surface part of the subducting plate ( $F_E$ ) (only for experiment 9), (d) bending force of the subducting plate ( $F_{Be}$ ), and (e) rollback-induced flow force ( $F_{RIF}$ ). For a discussion of the forces see text. Thick gray lines indicate the time when the slab tip hits the upper-lower mantle discontinuity.

determines the plate-perpendicular velocity gradient. The first part of equation (2) quantifies the shear force between the slab and the surrounding mantle ( $F_{SH}(s)$ ), while the second part quantifies the shear force between the horizontal surface part of the subducting plate and the underlying mantle ( $F_{SH}(h)$ ). For each experiment, the shear gradient was determined from measuring  $d\xi/dt$  for passive markers in the plate and passive markers in the underlying glucose syrup, located some 1–3 cm from the plate.  $d\xi/dt$  decreases approximately linearly with increasing distance from the bottom of the plate to  $\sim 0$  cm/hr at 4–5 cm below the bottom of the plate.  $d\xi/dt$  could be determined accurately for markers in the plate but less accurate for markers in the syrup with errors in the order of  $\pm 20\%$ . The magnitude of the shear forces is plotted in Figure 3b, showing a progressive increase with time until the slab tip hits the lower discontinuity. This increase results from the initial accelerated subduction followed by a slowdown when the slab tip starts to interact with the lower discontinuity.

[10] The extension force ( $F_E$ ) was calculated from the product of the extensional strain rate in the surface part of the subducting plate ( $\dot{\epsilon}_e$ ), the subducting plate viscosity ( $\eta_{sp}$ ), the plate width ( $W$ ), and the plate thickness ( $T$ ). The magnitude of  $F_E$  is plotted in Figure 3c for experiment 9 only, since no extension was observed in experiment 11. The curve shows an increase of  $F_E$  with time until the slab tip hits the lower discontinuity.

[11] The bending force was calculated from estimating the average strain rate observed at the hinge of the subducting plate for progressive time-steps. The strain rate was determined from the change in length of the subducting plate as it approached the hinge. Bending of the plate caused the convex side of the plate to experience extension and the concave side to experience shortening. From measuring the strain on both sides for progressive time-steps, an average bending strain rate ( $\dot{\epsilon}_b$ ) was obtained.  $F_{Be}$  could then be calculated as follows:

$$F_{Be} = \eta_{sp} \dot{\epsilon}_b WT \quad (3)$$

Measuring  $\dot{\epsilon}_b$  was somewhat inaccurate, with errors up to  $\pm 30\%$ . Therefore, the development of  $F_{Be}$  in Figure 3d is not as straightforward as for the other forces in Figure 3. However, the data do suggest that  $F_{Be}$  increases with time. Tentative linear curves have been plotted in Figure 3d, although non-linear curves can be fitted as well. The experiments show that  $F_{Be}$  comprises a large part ( $\sim 15$ – $30\%$ ) of  $F_B$  (decreasing from  $\sim 28\%$  and  $22\%$  to  $\sim 15\%$  and  $16\%$  for experiment 9 and 11 respectively).

[12] The rollback-induced flow force ( $F_{RIF}$ ) was difficult to quantify, since the flow pattern due to slab retreat is complex [Schellart, 2003]. It can be quantified indirectly from equation (1a) and (1b), since all the other components in this equation are roughly known. The resulting graphs



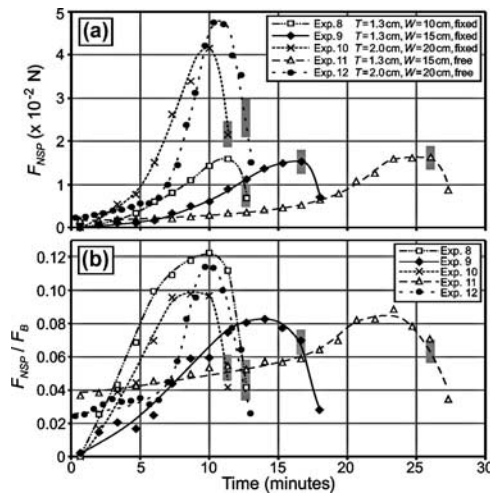


**Figure 4.** Diagrams illustrating (a) development of the net slab pull force ( $F_{NSP}$ ) and (b) development of the net slab pull force to buoyancy force ratio ( $F_{NSP}/F_B$ ) for five experiments. Thick gray lines indicate the time when the slab tip hits the upper-lower mantle discontinuity.  $T$  is slab thickness,  $W$  is slab width, and fixed and free stand for fixed and free trailing edge, respectively.

have been plotted in Figure 3e, showing that  $F_{RIF}$  increases in a similar fashion as  $F_B$ ,  $F_{SH}$  and  $F_E$ . This is not surprising, since the resistance to flow is related to the product of the average slab-perpendicular velocity ( $v_{\perp,av}$ ) and slab length ( $L_s$ ), which is directly related to  $F_B$ . In addition, the resistance to flow is related to the product of the slab width ( $W$ ) and the slab-perpendicular velocity of the slab tip ( $v_{\perp,tip}$ ). The resistance to flow can be approximated as follows:

$$F_{RIF} \approx C\eta_m SL_c \{ (2v_{\perp,av}L_s) + (v_{\perp,tip}W) \} \quad (4)$$

where  $C$  is a constant;  $S$  is a parameter related to the shear gradient in the mantle; and  $L_c$  is a parameter related to the magnitude of the flow cell. The aforementioned three quantities are unknown for the experiments, but remain constant during an experiment, while  $\eta_m$  is known. The remaining parameters in equation (4) can be deduced from the experiments. With an optimized value for  $CSL_c$ , the data plot relatively close to the curve as deduced from equation (1a), as shown for experiment 9 ( $CSL_c = 33$ ) and 11 ( $CSL_c = 53$ ) in Figure 3e. This suggests that the remainder of  $F_B$  is indeed mainly absorbed by  $F_{RIF}$ . The divergence of the data and the curves, as can be observed for  $t \geq 14$  minutes in experiment 9, results from interaction of the slab and flow cells with the upper-lower mantle discontinuity. Calculations for experiment 9 and 11 show that  $F_{RIF}$  comprises a large part (68–73%) of  $F_B$  from the initiation of subduction until the slab starts to interact with the discontinuity.

[13] The net slab pull force can be calculated from equation (1b).  $F_{NSP}$  is plotted in Figure 4a for experiment 9 and 11 and three other experiments with different plate dimensions. The results show that the lithosphere acts as a stress guide and pulls the surface part of the lithosphere into the subduction zone, as was predicted earlier [e.g.,

Elsasser, 1971]. For all experiments,  $F_{NSP}$  increases with time until a maximum value is reached, and then starts to decline. This decline is most likely related to the increased force needed to deform the plate as it approaches the bottom. Experiment 10 and 12 have the highest values, resulting from a thicker slab (2.0 cm) and therefore greater  $F_B$  compared to the other experiments (1.3 cm). In Figure 4b the  $F_{NSP}/F_B$  ratio is plotted, showing an increase until a maximum value is reached with a slab length corresponding to  $\sim 350$ – $650$  km and a slab dip of  $55$ – $80^\circ$ .  $F_{NSP}/F_B$  increases from  $\sim 0$ – $4\%$  to a maximum of  $\sim 8$ – $12\%$  for all experiments. This increase is closely linked to the increase in slab dip angle (from  $15$ – $30^\circ$  to a maximum of  $55$ – $80^\circ$ ). Calculations for experiments 9 and 11 indicate that the remainder of  $F_B$  is mainly used to drive rollback-induced mantle flow ( $\sim 70\%$ ), to bend the subducting plate ( $\sim 15$ – $30\%$ ) and to drive shearing between slab and mantle ( $\sim 0$ – $8\%$ ).

## 5. Discussion and Conclusions

[14] Investigations from Conrad and Lithgow-Bertelloni [2002] suggest that for upper mantle subduction  $F_{NSP}/F_B \approx 70$ – $100\%$ , which is significantly more than found here. The difference might be due to the vertical style of subduction in their models, in which slab rollback was not allowed. In such a scenario, the surrounding mantle supports the slab only by shear stresses. However, if subduction would be allowed at a non-vertical subduction angle and if slab rollback would be allowed, then the mantle would support the slab by additional viscous stresses, i.e., stresses needed to drive rollback-induced flow in the mantle. One would then expect much less than  $70$ – $100\%$  of  $F_B$  to be transmitted as  $F_{NSP}$ .

[15] The results indicate that  $F_{NSP}$  is an order of magnitude smaller than  $F_B$ . However, a simple calculation shows that with an  $8$ – $12\%$  effectiveness of stress transmission, a  $650$  km long and  $100$  km thick slab, a slab dip angle  $>55^\circ$ , and  $\Delta\rho \approx 80$  kg/m<sup>3</sup> ( $\Delta\rho$  from Cloos [1993]), then  $F_{NSP}$  is  $\sim 4.1$ – $6.1 \times 10^{12}$  N/m ( $\sim 41$ – $61$  MPa). This makes  $F_{NSP}$  about twice as large as the ridge push force ( $\sim 2$ – $3 \times 10^{12}$  N/m).

[16] Such calculations could explain why several plates (Pacific, Philippine, Nazca, Cocos and Indo-Australian plates) move more rapidly ( $\sim 5$ – $10$  cm/yr) than other plates ( $\sim 0$ – $3$  cm/yr) [Gripp and Gordon, 1990]. First, because a large part of the circumference of the fast plates is attached to a subduction zone ( $\sim 25$ – $40\%$ ) [Forsyth and Uyeda, 1975; Gripp and Gordon, 1990]; And second, because the slab length at these subduction zones is relatively large ( $>300$ – $400$  km [Yokokura, 1981]), resulting in a large  $F_B$  and a high  $F_{NSP}$ . The fastest plate (Pacific plate,  $\sim 10$  cm/yr) has the longest ( $300$ – $1200$  km) and oldest (Cretaceous–Jurassic) and therefore densest slabs attached, which dip at steep angles ( $30$ – $85^\circ$  [Yokokura, 1981]), resulting in a large  $F_{NSP}$ . This could explain why the Pacific plate is moving faster than the other relatively fast plates, which have either a smaller dip angle, shorter slab, young age, or a combination of these factors.

[17] **Acknowledgments.** I thank M. Sandiford, C. Kincaid, L. Moresi, V. Toy, J. Braun, G. Rosenbaum, D. Giles and two anonymous reviewers for helpful comments.

## References

- Artyushkov, E. V. (1983), *Geodynamics*, 312 pp., Elsevier Sci., New York.
- Cloos, M. (1993), Lithospheric buoyancy and collisional orogenesis: Subduction of oceanic plateaus, continental margins, island arcs, spreading ridges and seamounts, *Geol. Soc. Am. Bull.*, *105*, 715–737.
- Conrad, C. P., and B. H. Hager (1999), Effects of plate bending and fault strength at subduction zones on plate dynamics, *J. Geophys. Res.*, *104*, 17,551–17,571.
- Conrad, C. P., and C. Lithgow-Bertelloni (2002), How mantle slabs drive plate tectonics, *Science*, *298*, 207–209.
- Davies, G. F., and M. A. Richards (1992), Mantle convection, *J. Geol.*, *100*, 151–206.
- Elsasser, W. M. (1971), Sea-floor spreading as thermal convection, *J. Geophys. Res.*, *76*, 1101–1112.
- Forsyth, D. W., and S. Uyeda (1975), On the relative importance of the driving forces of plate motion, *Geophys. J. R. Astron. Soc.*, *43*, 163–200.
- Fukao, Y., S. Widiyantoro, and M. Obayashi (2001), Stagnant slabs in the upper and lower mantle transition region, *Rev. Geophys.*, *39*, 291–323.
- Garfunkel, Z., C. A. Anderson, and G. Schubert (1986), Mantle circulation and the lateral migration of subducted slabs, *J. Geophys. Res.*, *91*, 7205–7223.
- Gripp, A. E., and R. G. Gordon (1990), Current plate velocities relative to the hotspots incorporating the NUVEL-1 global plate motion model, *Geophys. Res. Lett.*, *17*, 1109–1112.
- Gurnis, M., and B. H. Hager (1988), Controls of the structure of subducted slabs, *Nature*, *335*, 317–321.
- Houseman, G. A., and D. Gubbins (1997), Deformation of subducted oceanic lithosphere, *Geophys. J. Int.*, *131*, 535–551.
- Jacoby, W. R. (1973), Model experiment of plate movements, *Nature (Physical Science)*, *242*, 130–134.
- Parsons, B., and F. M. Richter (1980), A relation between the driving force and geoid anomaly associated with mid-ocean ridges, *Earth Planet. Sci. Lett.*, *51*, 445–450.
- Ranalli, G. (1995), *Rheology of the Earth*, 413 pp., Chapman and Hall, New York.
- Schellart, W. P. (2003), Subduction rollback, arc formation and back-arc extension, Ph.D. thesis, Monash Univ., Melbourne, Australia.
- Yokokura, T. (1981), On subduction dip angles, *Tectonophysics*, *77*, 63–77.

---

W. P. Schellart, Research School of Earth Sciences, The Australian National University, Canberra, ACT 0200, Australia. (wouter.schellart@anu.edu.au)